Monolithic two-terminal tandem solar cells using Sb_2S_3 and solution-processed PbS quantum dots achieving an open-circuit potential beyond 1.1 V

Selina Kern [1], Gyusang Yi [1, 2], Pascal Büttner [1], Florian Scheler [1, 3], Minh-Hoa Tran [1], Sofia Korenko [1], Katharina E. Dehm [1], Ivan Kundrata [1], Steve Albrecht [3], Julien Bachmann[,1], Ryan W. Crisp*[,1]*

[1] Friedrich-Alexander-Universität Erlangen-Nürnberg, Chemistry of Thin Film Materials, Department of Chemistry and Pharmacy, Cauerstr. 3, 91058 Erlangen, Germany.

[2] Current address: Leibniz-Institut für Polymerforschung Dresden e.V., Institute of Physical Chemistry and Polymer Physics, Hohe Strasse 6, 01069 Dresden, Germany.

[3] Perovskite Tandem Solar Cells, Helmholtz-Zentrum Berlin für Materialien und Energie GmbH, 12489 Berlin, Germany.

KEYWORDS

Multijunction, chalcogenide solar cells, antimony sulfide, lead sulfide, nanocrystals, atomic layer deposition, recombination layer, mapping ellipsometry

ABSTRACT

Multijunction solar cells show the prospect to raise the theoretical efficiency limit of single junction solar cells by minimizing transmissive losses of large bandgap and emissive losses of lower bandgap absorber solar cells. In solar cell applications, Sb_2S_3 is considered an attractive absorber due to its elemental abundance, stability, and high absorption coefficient in the visible range of the solar spectrum, yet with a band gap of 1.7 eV it is transmissive for near-IR and IR photons. Using it as the top cell inside a tandem solar architecture in combination with a bottom cell employing e.g., PbS quantum dots, which have an adjustable band gap suitable for absorbing longer wavelengths, is hence a promising approach to harvest the solar spectrum more effectively. In this work, these two subcells are monolithically grown and connected in series by a poly(3,4-ethylene-dioxythiophene) polystyrene sulfonate (PEDOT:PSS)−ZnO tunnel junction as the recombination layer. We explore the surface morphology of ZnO QDs resulting from different spin coating conditions, which serve as the bottom cell's electron transport material. Furthermore, we examine the differences in photogenerated current upon varying the PbS QDs absorber layer thickness and the electrical and optical characteristics of the tandem with respect to the standalone reference cells. This tandem architecture demonstrates an extended spectral absorption into the IR with an open-circuit potential exceeding 1.1 V and a power conversion efficiency of 5.6%, projecting above the PCE of each single-junction cell.

INTRODUCTION

Generating electricity from sunlight and making it accessible to the public requires developing efficient and low-cost technologies that can effectively capture a broad range of the solar spectrum and reduce the area of sealed land involved in solar cell installation. Multi-junction solar devices that combine multiple p(-i)-n junctions with a staggered spectral response offer reduced spectral losses and, thus, can overcome the theoretically achievable efficiency limit of

33% calculated for single-junction solar cells. [1,2] Sb_2S_3 is considered a promising absorber material by combining relatively earth-abundant elements, high stability, and a notable absorption coefficient (1.8 x 10^5 cm^{-1} at 450 nm) [3] that makes it suitable for thin film optoelectronic applications. [4] However, despite its large band gap of 1.7 eV, a sizeable discrepancy is observed in the open-circuit potential (V_{OC}) being below 1 V for single-junction solar cells. This V_{OC} deficit is attributed to defect states in the absorber layer, leading to the self-trapping of charge carriers. [5] This not only limits the efficiency of the cells, but the large band gap also means there is a transmission of near-IR and IR photons that are lost for power conversion. Augmenting the spectral window in a tandem device with a second absorber to capture lower-energy photons can reduce the optical transmission related to the larger band gap absorber as well as the thermalization losses occurring for the lower band gap absorber, thus leading to an increased efficiency.

Based on calculations, a band gap of 1.7 eV paired with a second band gap of 1.1 eV can achieve a maximum power conversion efficiency of 45%. [6] For this reason, Sb_2S_3 has been theoretically considered a suitable top cell material for augmenting c-Si solar cells, yet a mismatch in cell performances has impeded experimental verification so far. [7] In another approach, Sb_2Se_3 represents a promising lower band gap material in an all-antimony chalcogenide tandem device for having a similar crystal structure, material properties, and equal stability as its sulfurous analog. A mechanically stacked four-terminal tandem configuration has been reported with increased overall efficiency compared to each subcell. [8] This device configuration allows the most relaxed process conditions, since the subcells can be prepared separately and are electrically connected afterwards. However, this causes additional material costs for encapsulating laterally conductive glass and the external electrical connections of the

subcells. A monolithic two-terminal configuration minimizes additional encapsulation materials and integration steps [9] since both subcells are deposited directly on top of each other representing a more attractive prospect for low-cost fabrication. However, a monolithic two-terminal all-antimony-chalcogenide tandem cell has been experimentally difficult so far, given the current high-temperature processing and annealing conditions, making it incompatible with the other employed materials. Therefore, they remained only conceptual until more advanced processing conditions can be found. [10]

Along the lines of milder processing conditions, a candidate that is proposed as a lower band gap absorber for Sb_2S_3 solar cells, are colloidal metal sulfide quantum dots (QDs), namely PbS. Due to quantum confinement, the band gap of PbS QDs can routinely be adjusted between 0.7 eV and 2 eV by altering the average size of the crystals, thereby tuning the spectral absorption range allowing to match the properties of the QDs with the conditions of the tandem cell. With solution-based processing methods under ambient conditions, colloidal QDs offer comparatively milder deposition conditions to avoid damaging underlying layers and to meet the requirements for a low-cost multijunction tandem configuration. [11]

To connect the two subcells in a two-terminal monolithic tandem solar device, a recombination layer is introduced. At this recombination layer, opposite charge carriers arrive from the two subcells and are recombined, closing the internal circuit, and linking the cells electrically in series as well as mechanically as they are deposited on top of each other. Finding a process-compatible and transparent recombination layer is critical for an efficiently working tandem cell. There are already options reported in the literature. Both Choi *et al.* [12] and Shi *et al*. [13] employed a thin layer of Au and ZnO on top of a p-type semiconductor and found that Au can mitigate an energetic offset between ZnO and the p-type semiconductor, facilitating recombination. Bi *et*

al. [14] used a thin layer of graphene that provided high transparency and conductivity to reduce optical and electrical losses. Wang *et al.* [15] introduced a tripartite recombination layer consisting of MoO_3/ITO/AZO with graded work functions to ensure minimum barriers for electron transport and recombination with holes.

In our study, we employ Sb_2S_3 as a top cell and PbS QDs as a bottom cell absorber in a monolithic two-terminal multijunction superstrate device. The structure for the top cell (glass/FTO/ZnO (ALD)/TiO_2/ZnS/Sb_2S_3/P3HT/PEDOT:PSS/Au) is adapted from Büttner *et al.* [16] with a double electron transport material (ETM) consisting of TiO_2 and ZnO deposited from atomic layer deposition (ALD) [17] to reduce the occurrence of pinholes and facilitate electron extraction from the absorber. Poly(3-hexylthiophene-2,5-diyl) (P3HT) and poly(3,4-ethylene-dioxythiophene) polystyrene sulfonate (PEDOT:PSS) serve as hole transport materials (HTM). The PbS bottom cell (when fabricated as a standalone) incorporates the stack of (glass/ITO/ZnO (QDs)/PbS-TBAI/PbS-EDT/MoO_3/Au) where tetrabutylammonium iodide (TBAI) and 1,2-ethanedithiol (EDT) are used for a post-deposition inorganic and organic ligand exchange that shifts the Fermi-level and band positions of the absorber [18,19] to enhance charge carrier transport and extraction. We introduce a thin layer of ZnO deposited by ALD to connect the subcells efficiently with a concept adapted from Crisp *et al.* [20] to create a highly doped p-n junction that favors the tunneling of the electrons and recombination with holes on the other side of the junction. This layer provides the advantages of being easy to deposit, stable, thin, and transparent in the visible and IR region, as well as protecting the underlying layers. [21] A scanning electron micrograph overlaid with a schematic presentation of the full tandem stack can be found in Figure 1. We focus on optimizing the PbS subcell by varying the absorber thickness and the process conditions for the ZnO QDs which serve as an ETM to achieve current matching. We

evaluate the current-voltage behavior of the tandem to understand its performance under illumination and obtain a series-connected device with a V_{OC} of 1135 mV which corresponds to the sum of the V_{OC} of the standalone subcells. With an overall short-circuit current density (J_{SC}) of 9.81 mA cm^{-2}, the tandem device achieves a power conversion efficiency (PCE) of 5.6%.

RESULTS AND DISCUSSION

We synthesized PbS QDs with a band gap of 1.2 eV indicated by the maximum value of the first exciton peak (Figure S1) and incorporated them in single-junction devices to test their performance under AM1.5 illumination. The optimization of the bottom cell addressed the morphology of the ZnO QDs used as ETM and the absorber layer thickness before incorporation into a tandem configuration to match the current between the subcells and enable voltage addition through a series connection.

The colloidal nature of QDs complicates the formation of a homogenous thin film that is required for proper carrier extraction and transport. Films of ZnO QDs suffer from a decreasing conductivity with increasing film thickness. Static spin-coating of the ETM, as opposed to dynamic, with the more volatile solvent chloroform ($CHCl_3$) leads to rough, porous films with irreproducible thickness as illustrated by imaging ellipsometry measurements in Panel A of Figure 2. By depositing the ETM dynamically from a solvent mixture of $CHCl_3$ with the slower drying methanol (MeOH) ($CHCl_3$/MeOH, 1:1, vol:vol), smoother and thinner complete layers can be formed. The X-ray diffractogram in Figure S2 indicates the formation of a zincite crystal structure with reflexes that are slightly broadened compared to a continuous layer of ZnO deposited by ALD.

Exploring the performance of the bottom cell to achieve current-matching conditions in a tandem architecture, a series of PbS single-junction cells was prepared with different thicknesses, resulting from varying the number of PbS-TBAI layers from two to six with two layers of PbS-EDT kept constant. For a complete understanding of the conditions necessary to exactly match the current would require a full optical model of the device stack as discussed in Ref. 22. However, to limit the number of adjustable parameters, we chose to vary the PbS thickness alone as its response does not strongly couple to performance of the Sb_2S_3 (i.e., changing the PbS thickness does not strongly affect the Sb_2S_3 response whereas changing the Sb_2S_3 drastically changes the light reaching the PbS thereby coupling these parameters). Figure S2 displays the X-ray diffractogram of PbS QDs that conform to the galena phase. The *JV*-curves in Panel B of Figure 2 demonstrate that two layers of PbS-TBAI result in films that cannot capture enough light and lead to a current response too low to match the Sb_2S_3 cell. Yet, the thickness after depositing six layers exceeds the diffusion length of charge carriers and prevents their extraction due to recombination. [18] The current response is consistently the highest between three and five layers; thus, three layers are employed in the tandem device since it requires the least material. The average values for J_{SC}, V_{OC}, Fill Factor (FF), and PCE with the different PbS thicknesses are tabulated in Table S1.

The collection and recombination of opposite charge carriers from the subcells happens at the PEDOT:PSS/ZnO (ALD) tunnel junction which allows the series connection. The recombination layer was investigated on top of the Sb_2S_3 standalone cell with the structure FTO/ZnO (ALD)/TiO_2/ZnS/Sb_2S_3/P3HT/PEDOT:PSS/ZnO (ALD)/Au and the current-voltage characteristics are presented in Panel C of Figure 2, overlayed with the curve of the standard Sb_2S_3 cell. A summary of the device performances is presented in Table S2. A visible decline in

V_{OC} is observed that is attributed to a decreased Fermi-level splitting due to n-type ZnO in contact with the p-type HTM. To test if a current decrease could originate from a higher series resistance of the recombination junction, a detached stack of ITO/PEDOT:PSS/ZnO (ALD)/Au was prepared, showing ohmic current-voltage behavior. From the line in Figure S3, a series resistance of ~1.5 Ω cm^2 across the stack can be determined. Considering the very thin layers of the junction with ~20 nm of PEDOT:PSS and ~15 nm of ZnO (ALD), a current decrease due to the recombination tunnel junction is unlikely also evidenced by similar J_{SC} values.

Panel A of Figure 3 shows *JV*-curves under AM1.5 illumination for the tandem cell, as well as for the Sb_2S_3 and PbS single-junction cells of the equivalent batch. All parameters, namely J_{SC}, V_{OC}, FF and PCE can be found in Table 1. The voltage of the tandem corresponds to the sum of its subcells, as expected from its monolithic configuration. Furthermore, the current is limited by the subcell producing the lower current. Here this means that the J_{SC} value is slightly lower than that of the standalone Sb_2S_3 subcell, since the Sb_2S_3 cell no longer benefits from the back reflection of the top metal contact – a process described in the optical modeling presented in Refs. 17 and 20. The dashed curves displaying the *JV*-behavior in the dark illustrate the cells' rectifying properties. Discrepancies are observable between the shape of the light and dark curves of the tandem cell with a visible cross-over. This indicates the occurrence of light-activated processes such as photodoping of a transport layer that result in different behavior of the tandem diode and solar cell. Considering the *JV*-behavior of the standalone single junction solar cells, light activation is required for the PbS subcell where analog discrepancies between light and dark curves are observed. In the tandem cell, the Sb_2S_3 subcell filters UV and visible light above its bandgap narrowing the illumination of the PbS subcell and impeding full light activation of the subcell thereby increasing the differences between light and dark behavior of

the tandem. Furthermore, a higher current with negative biases in the light curve of the PbS cell reflects current losses, resulting in a lower FF with respect to the other cells. The trend of the diode curves becomes more prominent when plotting the dark current on a semi-logarithmic scale (Panel B of Figure 3). The PbS diode reveals apparent current losses that are larger by four orders of magnitude than in the other cells due to a lower shunt resistance. Interestingly, the tandem diode does not appear to be overly affected by the current losses as expected from the PbS subcell. In comparison, the tandem cell presents a higher shunt resistance than the PbS diode though still lower than the Sb_2S_3 diode.

The spectral response of the tandem device was determined by its external quantum efficiency (EQE) characterized with different light biases designed to properly activate each cell and thereby examine each subcell separately. As a reference, the EQE spectra of the single-junction cells are presented in Panel C of Figure 3. With a band gap of 1.7 eV, Sb_2S_3 absorbs light with wavelengths below ~730 nm. Photonic losses at 380 nm and 600 nm are associated with parasitic absorption of ZnO [17] and P3HT [23], respectively. The absorption range of PbS is extended into the IR with a visible excitation peak at ~1100 nm. A decrease in quantum efficiency at 360 nm is caused by the parasitic absorption of ZnO QDs (the corresponding UV-vis spectra of the PbS and ZnO QDs can be found in Figure S1). In Panel D of Figure 3, two different scans are performed while illuminating the cell with light of individual wavelengths chosen to deconvolute the responses of the subcells. With a red-light bias (850 nm), the EQE spectrum follows that of the standalone Sb_2S_3 reference cell. Signals below the band gap could be caused by a spurious signal from the bias light activating the Sb_2S_3 subcell also leading to cross-talk between the cells. Applying a blue-light bias (455 nm), the spectral response from the PbS subcell shows the first exciton peak at ~1100 nm and two further peaks at 840 nm and 690 nm. The last two peaks are

attributed to optical constructive interferences. The integrated currents from the spectra for each subcell both approach the J_{SC} obtained from the *JV*-curve. A lower integrated current for the Sb_2S_3 subcell suggests that the top cell is current limiting for the tandem cell. The integrated current of the Sb_2S_3 subcell being lower than expected could also hint at degradation associated with the organic HTMs P3HT and PEDOT:PSS.

Impedance spectroscopy was performed to highlight some features of the charge transport and recombination mechanisms. The data were recorded under both dark conditions and AM1.5 sun illumination with an applied alternating voltage (dV = 10 mV/s) in the frequency range of 1 – 10000 Hz. The physical processes in Sb_2S_3 solar cells of the employed architecture are described by the series resistance (R_S) accounting for ohmic contact losses in series with a parallel combination of the recombination resistance (R_{rec}) and geometric capacitance (C_{geo}) that describe the recombination process. The employed ZnS layer was reported to prevent the recombination of electrons from the ETM with holes at the interface, but it can also introduce an energetic barrier to electron injection with increasing layer thickness due to the insulating nature of ZnS. Therefore, an additional $R_{ZnS}C_{ZnS}$-circuit in series with R_{rec} is associated with the carrier transport in the cell. [24] In the PbS QD subcell charge transport happens *via* hopping of charge carriers between the QDs, which potentially complicates the analysis through additional capacitive elements. This would require adding an *RC* parallel connection associated with the recombination of carriers at the boundary of each nanoparticle to the model. Yet for highly conductive materials and high applied voltages, this can be simplified to a single *RC* circuit in series with a resistor. [25] Impedance data was recorded in the dark for the standalone Sb_2S_3 and PbS reference cells; the corresponding data and fits can be found in Figure S4. Both cells exhibit semicircles in the Nyquist plots with applied potentials forward to their open-circuit potentials.

The observed flattened shape for our Sb_2S_3 structure was previously described by Büttner *et al.*[24] and appears for higher thicknesses of ZnS. The resistances towards recombination through the device at 0 V is ~12 kΩ cm^2 and thus higher than the resistance through the PbS cell with ~8 kΩ cm^2.

Linear sweep curves before and after the impedance measurement of the tandem cell indicate stable performance of the cells (Figure S5). The equivalent circuit of the tandem cell presented in Panel A of Figure 4 is adapted from the series connection of the two subcells (labeled 1 and 2) with a *RC* element representing the recombination processes of each subcell. The series resistor R_s corresponds to the impact of contacts, wires, and the series resistance throughout the device. [26] Yet, a specific assignment of the elements to one or the other cell cannot be justified since the impedance responses of the standalone single-junction solar cells expect overlapping contributions of both subcells at frequencies higher than 10^2 Hz. Therefore, the overall response of the circuit is considered for qualitative evaluation between a tandem cell in the dark and under AM1.5 illumination. Substituting the capacitors with constant phase elements accounts for non-idealities and to fit not perfectly circular features in the Nyquist plot. The obtained parameters were used to calculate a pseudo-capacitance *C** according to Ref. 27. In agreement with the circuit model, the Nyquist plots in the dark (Panel B of Figure 4) exhibit two overlapping semicircles that merge at high voltages. With illumination, a flattened semicircle also suggests two features that merged and became indistinguishable (Panel C of Figure 4). All corresponding Bode phase and modulus plots and fits can be found in Figure S6. At 0 V, the total resistance of the tandem is ~13.5 kΩ cm^2 in the dark and thus slightly higher than the recombination resistances of the standalone subcells. As expected, the total resistance decreases upon forward biasing the cell with and without illumination since the injected current density increases

likewise [28] (Panel D of Figure 4). With illumination, more mobile charge carriers are available, reducing the resistance towards recombination by one order of magnitude. At short-circuit conditions (i.e., at 0 V), charge carriers flow through the diode and are collected by the external circuit. With forward bias, the rectifying diode accumulates charges at its p(-i)-n junctions, which transpires in Panel E of Figure 4 as a rise in capacitance. At the diode's turn-on voltage, a drop in capacitance is expected when opposite charged carriers are injected. [29] Under illumination, the photogenerated current density creates the built-in electric field, rather than in the dark, where an outside field needs to be applied. Charge carriers are extracted over the whole time only slowly increasing the accumulation of the extracted charges. This leads to an increase of the recombination and is also visible as a decrease in recombination resistance. A higher capacitance in the dark can indicate charge accumulation at another interface (apart from the p(-i)-n junctions) originating from a barrier in the diode as by mid-band gap states trapping charge carriers and acting as an additional capacitor. More mobile charge carriers upon illumination can fill trap states altering the characteristics of the diode and mitigating the additional barrier in the device decreasing the overall capacitance. This agrees with the observations in the *JV*-curves of the tandem cell with a crossing of the light and dark curves that indicated enhanced processes upon light activation compared to the dark curve. The origin of the barriers was expected within the PbS stack that showed similar light induced enhancements. Additionally, the impedance data of the standalone Sb_2S_3 single junction cell showing slightly depressed semicircles can indicate that charge injection is also slightly hindered by a too thick layer of ZnS.

CONCLUSION

In this work, we presented a monolithic two-terminal tandem architecture based on two low-cost absorber materials with both an increased open-circuit potential and a larger range of spectral absorption. We explored the effects of the absorber layer thickness of the bottom PbS cell with respect to its efficiency and spectral response. A thin recombination layer based on ZnO deposited by ALD connects the cells in series, leading to voltage addition. Thereby, the efficiency of the tandem exceeds the efficiencies of each standalone single-junction solar cell. Both a potential injection barrier due to the ZnS layer in the standalone Sb_2S_3 cell and a current leakage due to shunts in the standalone PbS cell were observed that led to a decrease in FF of the tandem. Improved behavior of the tandem cell upon illumination in comparison to dark conditions suggests light activated processes originating from the PbS subcell where similar behavior was observed. Addressing especially the source of the current leakage in the PbS subcell could improve the current extraction and facilitate current matching when integrated in a tandem cell. This also gives an opportunity to investigate further promising QD materials as the bottom cell absorber in the proposed tandem architecture. Overall, our study highlights the value of interface engineering and material research in the future with the prospect for low-cost and high-efficiency tandem solar cells.

METHODS

Sample preparation

Fluorine-doped tin oxide (FTO) substrates (Techinstro, sheet resistance 10 Ω sq^{-1}) for the Sb_2S_3 subcells and tandems were patterned by etching with Zn powder and HCl (2 M) for 15 min. The substrates were cleaned by sonication in Hellmanex III (2% in water), acetone,

isopropanol, and deionized water for 5 min each. As the last step, the slides were treated with UV-ozone for 30 min to remove organic contaminants immediately before further depositions were done. Identical steps were followed for indium tin oxide (ITO) coated glass substrates (Techinstro, sheet resistance 10 Ω sq^{-1}) for the PbS QD cells.

Material deposition

ZnO by ALD as either ETM or recombination layer. ZnO by ALD as either ETM or recombination layer ZnO was deposited in an Arradiance GEMStar-XT-R reactor connected to an N_2 glovebox. Diethylzinc (DEZ) (at room temperature (RT); 95%, abcr) and water (at RT; milliQ) served as precursors with N_2 as carrier gas. The deposition was performed with pulse, exposure, and purging times of 0.2, 50, and 70 s, respectively, per cycle at a chamber temperature of 120 °C. Serving as an ETM, ZnO was deposited in 200 cycles, resulting in a film thickness of ~40 nm. Subsequently, the layer was annealed on a hot plate in air for 30 min at 500 °C. As a recombination layer, 70 cycles were forming a 15 nm film of ZnO without any further post-treatment.

TiO_2 by RF magnetron sputtering. Approximately 50 nm of TiO_2 were deposited from a TiO_2 target (99.99%) at a power density of 2.5 W cm^{-2} at a base pressure of 1.3 x 10^{-4} Pa and a working pressure of 4.3 Pa (CRC 622 model, Torr International, Inc.). The obtained amorphous films were annealed in air at 500 °C for 45 min to yield the anatase crystal structure.

ZnS and Sb_2S_3 with a ZnO fixation layer by ALD. ZnS and Sb_2S_3 were deposited in a homemade hot-wall ALD reactor without breaking vacuum between depositions. The precursors were DEZ (at RT; 95 %, abcr), tris(dimethylamido)-antimony(III) ($Sb(NMe_2)_3$) (at 40 °C; 99.99%, Sigma Aldrich), and H_2S (at RT; 3% vol in N_2, Air Liquide) with N_2 used as the carrier

gas. ZnS was deposited by performing 9 cycles (~1 nm) of pulse, exposure, and purging times of 0.2, 30, and 40 s, respectively, with a chamber temperature of 150 °C. Subsequently, the chamber was cooled to 120 °C and 600 cycles (~35 nm) of Sb_2S_3 were deposited using pulse, exposure, and purging times of 0.2, 15, and 15 s, respectively. After the reaction chamber had cooled to RT, the substrates were put into a UV/ozone cleaner (Novascan PSD-UV4) for 1 min and were immediately reinserted into the reaction chamber for subsequent ZnO deposition that prevents the Sb_2S_3 from dewetting during annealing. [17] Again, the precursors were DEZ (at RT; 95%, abcr) and water (at RT; milliQ), and the deposition was performed for 200 cycles (~20 nm) with opening, exposure, and pumping times of 0.2, 15, and 15 s, respectively. Since Sb_2S_3 was obtained amorphous, the samples were annealed for 2 min at 300 °C in an N_2-glovebox to form the stibnite phase. Before further treatment, the ZnO layer was fully etched away in a solution of acetic acid (5% vol) for 2 min. The samples were then washed in another solution of acetic acid (3% vol) and twice in deionized water.

P3HT by spin-coating. A solution of P3HT (15 mg mL^{-1}, regioregular, Sigma Aldrich) in chlorobenzene (Merck) was stirred overnight at 60 °C under a dry N_2-atmosphere. 50 µL of the solution were spin-coated dynamically at 6000 rpm for 60 s. Subsequently, the samples were dried on a hot plate at 90 °C for 30 min under N_2 inert gas.

PEDOT:PSS by spin-coating. PEDOT:PSS (HTL Solar, Ossila) was filtered through a 45 µm Nylon syringe filter. For better adhesion, 170 µL of the solution was spread over the samples and allowed to sit for 12 s before spinning with an acceleration of 6000 rpm s^{-1} to 6000 rpm for 60 s. The samples were dried for 30 min at 90 °C in an N_2 atmosphere.

MoO_3 by thermal evaporation. An Angstrom Covap thermal evaporator integrated into an N_2-glovebox with an Inficon SQC-310C deposition controller was used for depositing MoO_3 (99.95% chunks and pieces from Angstrom Engineering). A shadow mask blocked the front FTO contacts and narrowed the deposition on the active area and the bottom contacts. The final thickness was set to 20 nm.

Metal contacts by thermal evaporation. The same Angstrom Covap device with an Inficon SQC-310C deposition controller was utilized for the metal contacts. The samples were masked leaving eight areas of 0.075 cm^2 uncovered. Au (99.99% pellets from m&k GmbH) was deposited with a final thickness of 80 nm.

Synthesis of ZnO QDs. The synthesis of ZnO QDs was adapted from Chuang *et al.* [30] Zinc acetate dihydrate (2.95 g, 13.4 mmol, Roth) was dissolved in MeOH (125 mL, Fischer chemical) and stirred at 60 °C. A solution of potassium hydroxide (1.48 g, 26.4 mmol, Roth) in MeOH (65 mL) was added dropwise to the stirred zinc acetate dihydrate solution and stirring was continued at 60 °C for 2.5 h. The ZnO QDs were centrifuged at 7500 rpm and washed with MeOH three times. After the last centrifugation, the precipitate was resuspended in $CHCl_3$ (15.0 mL) or a mixture of $CHCl_3$/MeOH (15.0 mL, 1:1) and filtered through a PTFE syringe filter (0.45 µm pore-size), aiming for a concentration of 95 mg mL^{-1}.

Synthesis of PbS QDs. PbS QDs were synthesized based on a method from Zhang *et al.* [31] Lead acetate (0.77 g, 99.99%, Sigma Aldrich), oleic acid (2.00 – 4.00 mL, 90.00%, Sigma Aldrich), and 1-octadecene (12.7 mL, 90.99%, Sigma Aldrich) were loaded in a flask and heated to 110 °C for 20 min under vacuum. The temperature was reduced to 90 – 95 °C. Bis(trimethylsilyl) sulfide (210 µL, synthesis grade, Sigma Aldrich) was diluted in 1-octadecene

(5.00 mL) and quickly injected into the solution. After the injection, the mixture was naturally cooled down to RT. The PbS QDs were centrifuged three times at 7500 rpm with added toluene and ethanol. After the last centrifugation, the precipitate was redispersed in octane at a concentration of 40 mg mL^{-1}.

QD Deposition. ZnO QDs were spin-coated dynamically at 3000 rpm and annealed at 60 °C to not damage the underlying tandem layer stack. PbS QD layers were fabricated by spin-coating at 1000 rpm. For a ligand exchange, a solution of TBAI in MeOH (10 mg mL^{-1}) was applied to the sample for 30 s and removed by spinning at 1000 rpm and rinsing with MeOH. These steps were repeated three times. Analogously, the last two layers of PbS were coated and treated with a solution of EDT in acetonitrile (10 mM), spun at 1000 rpm to dry, and rinsed with MeOH while spinning.

Device characterization

Current-voltage (*JV*) measurements. For photovoltaic characterization, the solar spectrum was simulated with a Xe lamp source calibrated to AM1.5 at 100 mW cm^{-2} with a reference Si solar cell (Newport). The electrical data were obtained from −0.3 to 1 V for single junction Sb_2S_3 and PbS cells and from −0.3 to 1.5 V for the tandem cells with a scan speed of 50 mV s^{-1} by a single-channel Gamry Reference 600 potentiostat.

External quantum efficiency (EQE) spectra of single junction solar cells. EQE spectra were recorded using an Oriel's QEPVSI-b system with a 300 W Xe light source, a monochromator, and a lock-in amplifier (Stanford Research Systems) for the single junction Sb_2S_3 and PbS cells which has a detector cut-off around 1120 nm. The EQE was integrated using the AM 1.5 spectrum over the range 300 to 1120 nm.

External quantum efficiency (EQE) spectra of tandem solar cells. EQE spectra of each subcell were recorded with a home-built setup using chopped (79 Hz) monochromatic light from a Xe and He lamp source in the wavelength range from 300 – 1200 nm. The probe light spot covered the full device active area. The bottom PbS cell was measured by saturating the top Sb_2S_3 cell using a blue LED with 455 nm peak emission to maintain short circuit conditions. For the Sb_2S_3 top cell measurement, a NIR LED with 820 nm peak emission was used.

Electrochemical impedance spectroscopy (EIS). The measurements were performed using a Gamry Interface 1000 potentiostat in the dark from −0.2 to 0.7 V for the Sb_2S_3 subcells and from −0.2 to 1.3 V for the combined tandem cells. The electrical data from the Mott–Schottky plots were obtained at a frequency of 10 kHz in the dark from −0.2 to 1.2 V.

Spectroscopic ellipsometry. The thicknesses of layers deposited by ALD and sputter coating were measured on silicon wafers (with native oxide or including a 200 nm thermal oxide layer) using a Sentech (SENpro) ellipsometer.

Mapping ellipsometry. The topography of ZnO layers was investigated with an EP4 Imaging Ellipsometer equipped with a DCC camera (Accurion GmbH). The thickness maps were recorded over an area of 112.9 µm x 151.1 µm using a 50x objective (Nikon), measuring at six distinct wavelengths (385, 447, 523, 595, 658, and 841 nm) with an incident angle of 60°. The acquired data was fitted with the EP4 modelling software using the optical parameters (*n* and *k*) from Refs. [32,33] ZnO films from ZnO QDs were prepared as stated above. Si wafers with native oxide were used as a substrate.

X-ray diffraction (XRD) measurements. The diffractograms were obtained with a Bruker D8 Advance that incorporates a Cu Kα source and a Lynxeye XE-T detector.

Scanning electron microscopy (SEM). SEM micrographs were obtained with a JEOL JSM 6400 instrument equipped with a LaB6 cathode or a Zeiss Gemini 500 field-emission instrument.

FIGURES

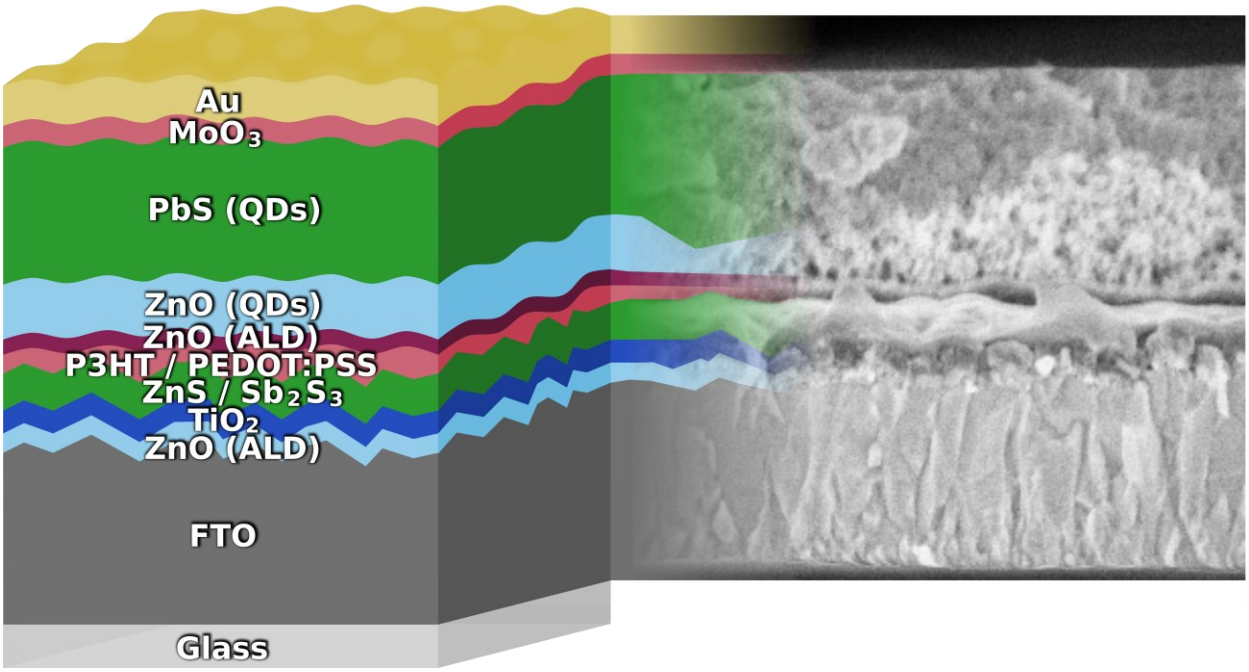

Figure 1. A) Scanning electron micrograph of an Sb_2S_3/PbS tandem cell without MoO_3/Au contact including a schematic representation of the full device structure.

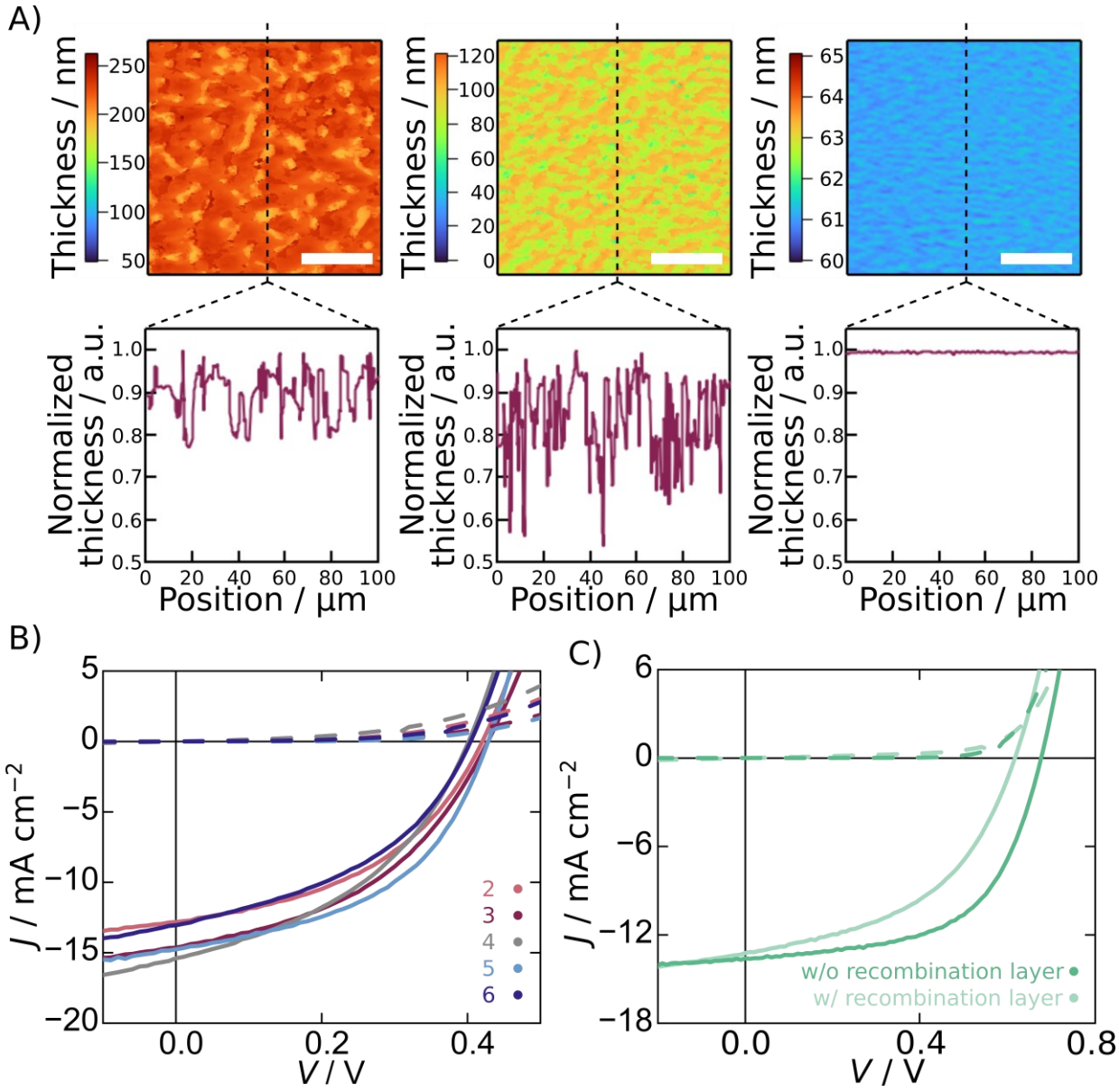

Figure 2. A) Thickness maps from imaging ellipsometry measurements with corresponding line scans taken at the indicated position with values normalized 0 to 1 to better compare the variations in thickness. All scale bars correspond to 25 µm. From left to right the deposition method is changed from statically spin coating the ZnO QDs (left) or dynamically (middle) from only $CHCl_3$, or dynamically from a mixture of $CHCl_3$/MeOH (1:1, vol:vol) (right). B) Current-voltage characteristics of PbS single-junction cells incorporating between two and six layers of PbS treated with TBAI. Two additional layers of PbS with a ligand exchange using EDT were kept constant. C) Current-voltage characteristics are presented for the standalone Sb_2S_3 cell with (light green) and without (dark green) an additional layer of ZnO (ALD) as a recombination layer for the tandem.

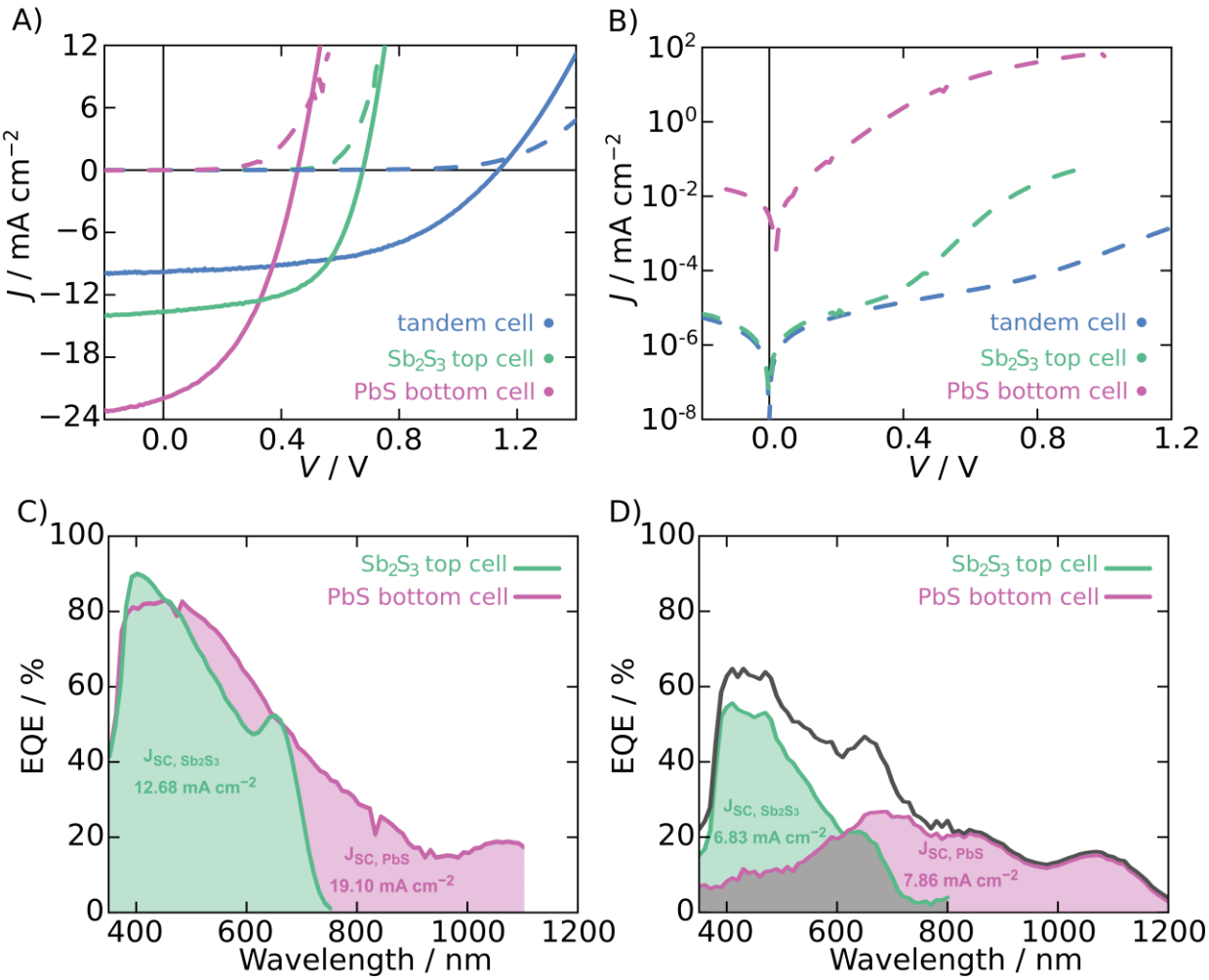

Figure 3. A) Current-voltage characteristics for a tandem device (blue) plotted together with the Sb_2S_3 (green) and PbS (pink) single-junction reference cells. The solid lines represent measurements under illumination, while the dashed lines are measurements in the dark. B) Dark current-voltage characteristics are plotted on a semi-logarithmic scale. C) External quantum efficiency of the standalone Sb_2S_3 and PbS cells with white light bias. D) External quantum efficiency measured with a red-light bias (850 nm) gives the decoupled spectral response of the Sb_2S_3 (green) subcell, whereas a blue-light bias (455 nm) is for measurement of the PbS (pink) subcell. The black line represents the sum of both curves.

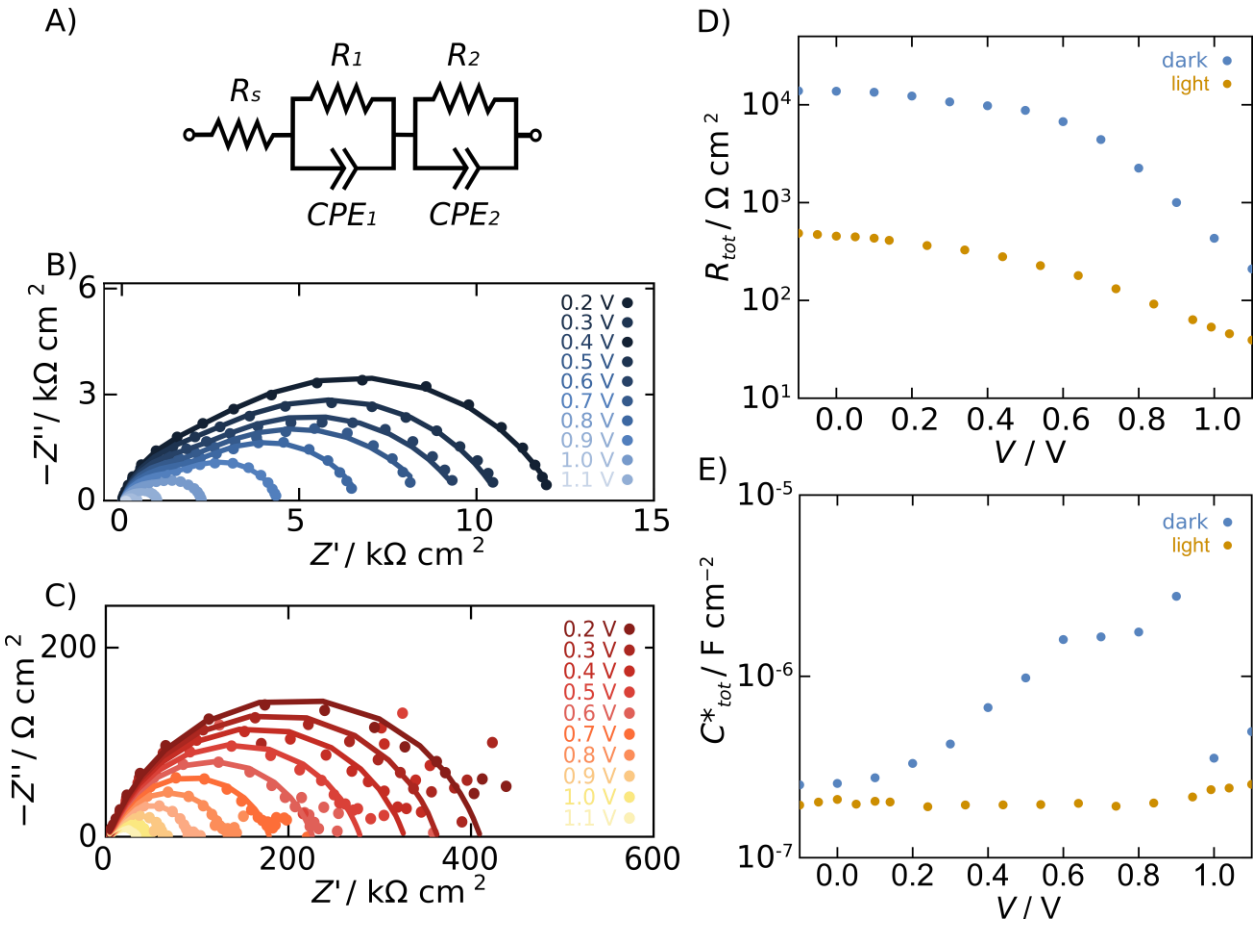

Figure 4. A) The equivalent circuit model to fit the electrochemical impedance spectroscopy data. Constant phase elements were used for more accurate fitting. B) The Nyquist plot shows the trend of the tandem cell impedance upon varying the applied potential between 0.20 and 1.10 V in the dark. The points represent experimental data overlaid with the corresponding fit as a solid line. C) Nyquist plot of the same tandem cell under AM1.5 illumination and an applied bias between 0.20 and 1.10 V. The points represent experimental data and the solid lines the corresponding fit. D) Trend of the total resistance on a semi-logarithmic scale that were obtained from the fits of the impedance data plotted against the applied voltage of the tandem cell in the dark (blue) and under AM1.5 illumination (yellow). E) Evolution of the total capacitance on a semi-logarithmic scale versus the applied voltage for the tandem cell in the dark (blue) and under AM1.5 illumination (yellow).

TABLES

Table 1. Summary of a representative device for each solar cell.

	J_{SC} (mA cm^{-2})	V_{OC} (mV)	FF	PCE (%)
tandem cell	9.81	1135	0.51	5.64
Sb_2S_3 cell	13.6	679	0.58	5.36
PbS cell	22.0	460	0.42	4.26

ASSOCIATED CONTENT

Supporting Information. A PDF file of the optical absorbance spectra, X-ray diffraction patterns of the materials, current-voltage plots of the tunnel junction and the tandem before and after EIS, Nyquist and Bode plots, Mott-Schottky analysis, and tabulated performance parameters for current-voltage plots is available.

AUTHOR INFORMATION

Corresponding Author

*Ryan W. Crisp Ryan.Crisp@fau.de

*Julien Bachmann Julien.Bachmann@fau.de

Author Contributions

The manuscript was written through contributions of all authors. All authors have given approval to the final version of the manuscript.

Funding Sources

This work was supported by the Profile Center "Engineering of Advanced Materials" (EAM) at FAU under a Starting Grant for RWC and by the Deutsche Forschungsgemeinschaft (DFG) - Project numbers 465220299 and 429730598.

Financial support from the following is acknowledged: HyperCells Graduate School, Helmholtz Association on EU-partnering project TAPAS, and HySPRINT Helmholtz Innovation Lab.

ACKNOWLEDGMENT

The authors thank Dr. Ignacio Mínguez-Bacho for SEM assistance and Dr. Sebastian Bochmann for XRD and SEM assistance.

We further thank the Kompetenzzentrum Photovoltaik Berlin (PVcomB) for providing access to their tandem EQE setup. In this regard, we want to thank especially T. Hänel (PVcomB, HZB) for technical assistance.

REFERENCES

(1) Shockley, W.; Queisser, H. J. Detailed Balance Limit of Efficiency of p-n Junction Solar Cells. *Journal of Applied Physics*, 1961. DOI: 10.1063/1.1736034.
(2) Rühle, S. Tabulated values of the Shockley–Queisser limit for single junction solar cells. *Solar Energy*, 2016. DOI: 10.1016/j.solener.2016.02.015.
(3) Versavel, M. Y.; Haber, J. A. Structural and optical properties of amorphous and crystalline antimony sulfide thin-films. *Thin Solid Films*, 2007. DOI: 10.1016/j.tsf.2007.03.043.
(4) Tang, R.; Wang, X.; Jiang, C.; Li, S.; Jiang, G.; Yang, S.; Zhu, C.; Chen, T. Vacuum assisted solution processing for highly efficient Sb 2 S 3 solar cells. *J. Mater. Chem. A*, 2018. DOI: 10.1039/C8TA05614E.
(5) Chen, C.; Tang, J. Open-Circuit Voltage Loss of Antimony Chalcogenide Solar Cells: Status, Origin, and Possible Solutions. *ACS Energy Lett.*, 2020. DOI: 10.1021/acsenergylett.0c00940.
(6) Meillaud, F.; Shah, A.; Droz, C.; Vallat-Sauvain, E.; Miazza, C. Efficiency limits for single-junction and tandem solar cells. *Solar Energy Materials and Solar Cells*, 2006. DOI: 10.1016/j.solmat.2006.06.002.
(7) Kondrotas, R.; Chen, C.; Tang, J. Sb2S3 Solar Cells. *Joule*, 2018. DOI: 10.1016/j.joule.2018.04.003.
(8) Zhang, J.; Lian, W.; Yin, Y.; Wang, X.; Tang, R.; Qian, C.; Hao, X.; Zhu, C.; Chen, T. All Antimony Chalcogenide Tandem Solar Cell. *Sol. RRL*, 2020. DOI: 10.1002/solr.202000048.
(9) Schnabel, M.; Rienacker, M.; Warren, E. L.; Geisz, J. F.; Peibst, R.; Stradins, P.; Tamboli, A. C. Equivalent Performance in Three-Terminal and Four-Terminal Tandem Solar Cells. *IEEE J. Photovoltaics*, 2018. DOI: 10.1109/JPHOTOV.2018.2865175.

(10) Cao, Y.; Zhu, X.; Jiang, J.; Liu, C.; Zhou, J.; Ni, J.; Zhang, J.; Pang, J. Rotational design of charge carrier transport layers for optimal antimony trisulfide solar cells and its integration in tandem devices. *Solar Energy Materials and Solar Cells*, 2020. DOI: 10.1016/j.solmat.2019.110279.
(11) Ganesan, A.; Houtepen, A.; Crisp, R. Quantum Dot Solar Cells: Small Beginnings Have Large Impacts. *Applied Sciences*, 2018. DOI: 10.3390/app8101867.
(12) Choi, J. J.; Wenger, W. N.; Hoffman, R. S.; Lim, Y.-F.; Luria, J.; Jasieniak, J.; Marohn, J. A.; Hanrath, T. Solution-processed nanocrystal quantum dot tandem solar cells. *Advanced materials (Deerfield Beach, Fla.)*, 2011. DOI: 10.1002/adma.201100723.
(13) Shi, G.; Wang, Y.; Liu, Z.; Han, L.; Liu, J.; Wang, Y.; Lu, K.; Chen, S.; Ling, X.; Li, Y.; et al. Stable and Highly Efficient PbS Quantum Dot Tandem Solar Cells Employing a Rationally Designed Recombination Layer. *Adv. Energy Mater.*, 2017. DOI: 10.1002/aenm.201602667.
(14) Bi, Y.; Pradhan, S.; Akgul, M. Z.; Gupta, S.; Stavrinadis, A.; Wang, J.; Konstantatos, G. Colloidal Quantum Dot Tandem Solar Cells Using Chemical Vapor Deposited Graphene as an Atomically Thin Intermediate Recombination Layer. *ACS Energy Lett.*, 2018. DOI: 10.1021/acsenergylett.8b00675.
(15) Wang, X.; Koleilat, G. I.; Tang, J.; Liu, H.; Kramer, I. J.; Debnath, R.; Brzozowski, L.; Barkhouse, D. A. R.; Levina, L.; Hoogland, S.; et al. Tandem colloidal quantum dot solar cells employing a graded recombination layer. *Nature Photon*, 2011. DOI: 10.1038/nphoton.2011.123.
(16) Büttner, P.; Scheler, F.; Pointer, C.; Döhler, D.; Barr, M. K. S.; Koroleva, A.; Pankin, D.; Hatada, R.; Flege, S.; Manshina, A.; et al. Adjusting Interfacial Chemistry and Electronic Properties of Photovoltaics Based on a Highly Pure Sb2S3 Absorber by Atomic Layer Deposition. *ACS applied energy materials*, 2019. DOI: 10.1021/acsaem.9b01721.
(17) Büttner, P.; Scheler, F.; Döhler, D.; Barr, M. K.; Bosch, M.; Rey, M.; Yokosawa, T.; Hinz, S.; Maultzsch, J.; Spiecker, E.; et al. Continuous, crystalline Sb2S3 ultrathin light absorber coatings in solar cells based on photonic concentric p-i-n heterojunctions. *Nano Energy*, 2022. DOI: 10.1016/j.nanoen.2022.107820.
(18) Crisp, R. W.; Kroupa, D. M.; Marshall, A. R.; Miller, E. M.; Zhang, J.; Beard, M. C.; Luther, J. M. Metal halide solid-state surface treatment for high efficiency PbS and PbSe QD solar cells. *Scientific reports*, 2015. DOI: 10.1038/srep09945.
(19) Grimaldi, G.; van den Brom, M. J.; Du Fossé, I.; Crisp, R. W.; Kirkwood, N.; Gudjonsdottir, S.; Geuchies, J. J.; Kinge, S.; Siebbeles, L. D. A.; Houtepen, A. J. Engineering the Band Alignment in QD Heterojunction Films via Ligand Exchange. *The journal of physical chemistry. C, Nanomaterials and interfaces*, 2019. DOI: 10.1021/acs.jpcc.9b09470.
(20) Crisp, R. W.; Pach, G. F.; Kurley, J. M.; France, R. M.; Reese, M. O.; Nanayakkara, S. U.; MacLeod, B. A.; Talapin, D. V.; Beard, M. C.; Luther, J. M. Tandem Solar Cells from Solution-Processed CdTe and PbS Quantum Dots Using a ZnTe-ZnO Tunnel Junction. *Nano letters*, 2017. DOI: 10.1021/acs.nanolett.6b04423.
(21) Crisp, R. W.; Hashemi, F. S. M.; Alkemade, J.; Kirkwood, N.; Grimaldi, G.; Kinge, S.; Siebbeles, L. D. A.; Ommen, J. R.; Houtepen, A. J. Atomic Layer Deposition of ZnO on InP Quantum Dot Films for Charge Separation, Stabilization, and Solar Cell Formation. *Adv. Mater. Interfaces*, 2020. DOI: 10.1002/admi.201901600.
(22) Kurtz, S. R.; Faine, P.; Olson, J. M. Modeling of two-junction, series-connected tandem solar cells using top-cell thickness as an adjustable parameter. *Journal of Applied Physics*, 1990. DOI: 10.1063/1.347177.

(23) Dang, M. T.; Wantz, G.; Bejbouji, H.; Urien, M.; Dautel, O. J.; Vignau, L.; Hirsch, L. Polymeric solar cells based on P3HT:PCBM: Role of the casting solvent. *Solar Energy Materials and Solar Cells*, 2011. DOI: 10.1016/j.solmat.2011.07.039.
(24) Büttner, P.; Scheler, F.; Pointer, C.; Döhler, D.; Yokosawa, T.; Spiecker, E.; Boix, P. P.; Young, E. R.; Mínguez-Bacho, I.; Bachmann, J. ZnS Ultrathin Interfacial Layers for Optimizing Carrier Management in Sb2S3-based Photovoltaics. *ACS applied materials & interfaces*, 2021. DOI: 10.1021/acsami.0c21365.
(25) Fabregat-Santiago, F.; Garcia-Belmonte, G.; Mora-Seró, I.; Bisquert, J. Characterization of nanostructured hybrid and organic solar cells by impedance spectroscopy. *Physical chemistry chemical physics : PCCP*, 2011. DOI: 10.1039/c0cp02249g.
(26) Huang, Z.; Natu, G.; Ji, Z.; Hasin, P.; Wu, Y. p-Type Dye-Sensitized NiO Solar Cells: A Study by Electrochemical Impedance Spectroscopy. *J. Phys. Chem. C*, 2011. DOI: 10.1021/jp205306g.
(27) Proskuryakov, Y. Y.; Durose, K.; Al Turkestani, M. K.; Mora-Seró, I.; Garcia-Belmonte, G.; Fabregat-Santiago, F.; Bisquert, J.; Barrioz, V.; Lamb, D.; Irvine, S. J. C.; et al. Impedance spectroscopy of thin-film CdTe/CdS solar cells under varied illumination. *Journal of Applied Physics*, 2009. DOI: 10.1063/1.3204484.
(28) Wang, H.; Wang, Y.; He, B.; Li, W.; Sulaman, M.; Xu, J.; Yang, S.; Tang, Y.; Zou, B. Charge Carrier Conduction Mechanism in PbS Quantum Dot Solar Cells: Electrochemical Impedance Spectroscopy Study. *ACS applied materials & interfaces*, 2016. DOI: 10.1021/acsami.6b03198.
(29) Willis, S. M.; Cheng, C.; Assender, H. E.; Watt, A. A. R. *Modified Mott-Schottky Analysis of Nanocrystal Solar Cells*. https://arxiv.org/pdf/1112.1623.
(30) Chuang, C.-H. M.; Brown, P. R.; Bulović, V.; Bawendi, M. G. Improved performance and stability in quantum dot solar cells through band alignment engineering. *Nature materials*, 2014. DOI: 10.1038/nmat3984.
(31) Zhang, J.; Crisp, R. W.; Gao, J.; Kroupa, D. M.; Beard, M. C.; Luther, J. M. Synthetic Conditions for High-Accuracy Size Control of PbS Quantum Dots. *The journal of physical chemistry letters*, 2015. DOI: 10.1021/acs.jpclett.5b00689.
(32) Weigand, C.; Crisp, R.; Ladam, C.; Furtak, T.; Collins, R.; Grepstad, J.; Weman, H. Electrical, optical and structural properties of Al-doped ZnO thin films grown on GaAs(111)B substrates by pulsed laser deposition. *Thin Solid Films*, 2013. DOI: 10.1016/j.tsf.2013.07.052.
(33) Herzinger, C. M.; Johs, B.; McGahan, W. A.; Woollam, J. A.; Paulson, W. Ellipsometric determination of optical constants for silicon and thermally grown silicon dioxide via a multi-sample, multi-wavelength, multi-angle investigation. *Journal of Applied Physics*, 1998. DOI: 10.1063/1.367101.